Published in final edited form as:

Nat Struct Mol Biol. 2009 October ; 16(10): 1063–1067. doi:10.1038/nsmb.1662.

Structural Basis for Auto-regulation of the Zinc Transporter YiiP

Min Lu, **Jin Chai**, and **Dax Fu**

Biology Department, Brookhaven National Laboratory, Upton, NY 11973

Abstract

Zinc transporters play critical roles in cellular zinc homeostatic control. The 2.9-Å resolution structure of the zinc transporter YiiP from *Escherichia coli* reveals a richly charged dimer-interface stabilized by zinc binding. Site-directed fluorescent resonance energy transfer (FRET) measurements and mutation-activity analysis suggest that zinc binding triggers hinge movements of two electrically repulsive cytoplasmic domains pivoting around four salt-bridges situated at the juncture of the cytoplasmic and transmembrane domains. These highly conserved salt-bridges interlock transmembrane helices at the dimer-interface, well positioned to transmit zinc-induced inter-domain movements to reorient transmembrane helices, thereby modulating coordination geometry of the active-site for zinc transport. The cytoplasmic domain of YiiP is a structural mimic of metal trafficking proteins and the metal-binding domains of metal-transporting P-type ATPases. The use of this common structural module to regulate metal coordination chemistry may enable a tunable transport activity in response to cytoplasmic metal fluctuations.

Zinc is the second most abundant transition metal in cells with a zinc quota in the sub-millimolar range. It is an essential element for cell growth and development1,2, yet excess zinc is highly cytotoxic3. Cellular zinc is largely associated with zinc-binding proteins, so that the free zinc concentration in the cytoplasm can be kept below the picomolar range to minimize its cytotoxic effects4. To provide ample supplies of cellular zinc and avoid excessive zinc accumulation at the same time, two distinct families of zinc transporters contribute to a delicate balance between zinc acquisition and removal. The ZRT, IRT-like proteins (ZIPs)5,6 and the cation diffusion facilitators (CDFs)7,8 facilitate zinc uptake into and efflux from the cytoplasm, respectively. Both ZIPs and CDFs are conserved in all living organisms from bacteria to plants and animals. Mammalian ZIPs form family 39 in the classification of solute carrier proteins (*SLC39*), while mammalian CDFs, also known as zinc transporters (ZnTs), belong to the *SLC30* family. These zinc transporters utilize transmembrane electrochemical potentials to drive Zn(II) transport across the membrane barrier in opposite directions. Among them, CDFs function as Zn(II)/proton antiporters9,10. Zinc-dependent expression of complementary zinc transporters is thought to control steady-state equilibrium of zinc fluxes around a homeostatic set point11. On the other hand, abrupt zinc over-loading may demand a fast-responding regulatory mechanism to prevent toxic zinc

Correspondence should be addressed to D.F. (dax@bnl.gov).

Accession codes Protein Data Bank: the atomic coordinates and structure factors of YiiP have been deposited with accession code 3H90.

exposure. A recent crystal structure of a CDF transporter YiiP hints at the possibility that cytoplasmic zinc may directly activate its efflux activity12. In particular, YiiP contains two cytoplasmic zinc binding sites that may serve as zinc sensors to control zinc efflux through a membrane-embedded active site13. It was shown *in vitro* that the active site of YiiP selectively binds Zn(II) or Cd(II), and translocates the bound metal ion across the membrane on a ~50 millisecond timescale14. Nevertheless, the cytoplasmic zinc binding sites were only partially resolved at 3.8-Å resolution, providing limited insights into how cytoplasmic zinc binding may allosterically regulate the active site for zinc transport.

All CDF transporters share a common two-modular architecture, consisting of a transmembrane domain (TMD) followed by a C-terminal domain (CTD) protruding into the cytoplasm15. Intriguingly, the CTD in YiiP adopts a metallochaperone-like fold, despite a lack of sequence homology13. Metallochaperones are cytoplasmic metal carrier proteins that deliver metal ions to various protein targets16, including the metallochaperone-like domains of metal-transporting P-type ATPases17. A metallochaperone and its transporter partner can dock their metallochaperone modules together for metal transfer at the metal donor-acceptor interface18. Emerging evidence suggests that the metallochaperone is a common structural module involved in metal trafficking and transport19. Mutations in the metallochaperone-like domains of P-type ATPases can give rise to genetic disorders of copper imbalance known as Menkes and Wilson diseases20. Polymorphisms in the CTD of a human CDF homolog, ZnT-821, have been associated with the risk of diabetes22–25. While the metallochaperone module has been the focus of extensive studies of intracellular metal trafficking26, its functional role in metal transport is still poorly understood. In this work, we seek to understand how the CTD in YiiP senses cytoplasmic zinc and responds with a regulated zinc transport activity. The atomic details revealed in our structure-function analysis suggest that inter-CTD movements in YiiP allosterically modulate coordination chemistry of the active site to enable a zinc-regulated zinc-transport mechanism.

RESULTS

Structure determination

We utilized mercury binding to strengthen TMD-TMD lattice contacts in YiiP crystals, since the conformational flexibility inherent to loosely packed TMDs was hypothesized as a root cause of poor X-ray diffraction. Ethyl mercury phosphate or thiomerosal binding to C127 on the TMD surface (Supplementary Fig. 1 online) was found to extend the diffraction limit beyond 2.9-Å resolution, accompanied by a change of crystal symmetry from space group $P222_1$ to $P2_1$. As YiiP crystals suffered severe radiation damage during data collection, 25 crystals were used to generate a merged dataset to 2.9-Å (Table 1). The structure was solved by single isomorphous replacement and anomalous scattering (SIRAS) phasing aided by molecular replacement (see **Methods** for details). The structural model was refined to an R_{free} of 27.7% and an R_{cryst} of 26.1% with good stereochemical quality27 (most favored 87.8%, additionally allowed 12.1% and generously allowed 0.1%). At this resolution, all protein sidechains in functionally important regions as well as many mainchain carbonyl groups were well resolved (Supplementary Figs. 2 and 3 online).

Unique helix packing in the transmembrane domain

The 2.9-Å YiiP structure reveals a Y-shaped dimeric architecture as described previously (Fig. 1a)13. This crystal structure is supported by available cross-linking data and consistent with a projection structure of YiiP in the lipid bilayer obtained by electron microscopic imaging28. Nonetheless, a distinctive pattern of interhelix packing in the TMD becomes apparent at 2.9-Å resolution. The six transmembrane helices (TM1-6) can be grouped into two sub-domains: TM1, TM2, TM4 and TM5 form a compact four-helix-bundle, whereas the remaining TM3 and TM6 crossover in an antiparallel configuration outside the bundle (Fig. 1b). TM3 is tilted away from TM2; consequently, one side of the TM3-TM6 pair embraces TM5 at one corner of the rectangle-shaped four-helix-bundle (Fig. 1c), while the other side projects highly conserved hydrophobic residues into the TMD-TMD interface to seal the bottom of the V-shaped void (Fig. 1b). The orientation of the TM3-TM6 pairs is stabilized by four interlocked salt-bridges formed between Lys77 of TM3 and Asp207 from a short loop that connects TM6 to CTD (Fig. 1d). These highly conserved charged residues are arranged in a circular fashion to form a $(Lys77\text{-}Asp207)_2$ charge interlock (Fig. 1d and Supplementary Fig. 4 online) that bundles together the cytoplasmic ends of two TM3-TM6 pairs at the dimer interface.

Zinc binding sites with distinct coordination environments

Each YiiP protomer contains three zinc binding-sites with distinct coordination chemistry (Fig. 1a). The active-site for zinc transport14 (site A) is located toward the center of TMD (Fig. 2a), whereas two cytoplasmic binding sites, sites B and C, are localized to the TM2-TM3 connecting loop on the cytoplasmic membrane surface (Fig. 2c) and to the CTD-CTD interface (Fig. 2d), respectively. Among the three binding-sites, only sites A and C are conserved (Supplementary Fig. 5 online). Site A consists of four coordinating residues, Asp45, Asp49 from TM2, and His153, Asp157 from TM5. They form a coordination system with four ligand groups (Asp45 Oδ1, Asp49 Oδ2, His153 Nε2 and Asp157 Oδ2) positioned at vertexes of a nearly ideal tetrahedron (Fig. 2b). Tetrahedral coordination is preferred for Zn(II) and Cd(II) as opposed to octahedral for most other divalent cations. This observation is consistent with an earlier finding that site A can bind Zn(II) and Cd(II), but not Fe(II), Mg(II), Ca(II), Mn(II), Co(II) and Ni(II)14. Overexpression of YiiP was shown to render an *Escherichia coli* mutant strain more tolerant to iron exposure29, but whether YiiP is a *bona fide* ferrous iron efflux facilitator (FieF) remains controversial14.

Site A is confined exclusively between TM2 and TM5. A small TM2-TM5 shift could lead to a large readjustment of zinc coordination geometry (Fig. 2b). Therefore, a TM2-TM5 reorientation could effectively regulate the active-site either in favor of zinc binding or release. Remarkably, all four coordinating residues in site A are completely free of outer-shell constraints. These structural features appear well suited for rapid on-off switching of zinc coordination, as no making or breaking of outer shell interactions is needed for Zn(II) binding and release during a transport cycle. Thus the ensuing conformational flexibility of the active-site may contribute to a rapid Zn(II) turnover rate (Supplementary Table 1 online), which is several orders of magnitudes faster than Zn (II) exchange rates for typical zinc metalloproteins30. In sharp contrast, site C is characterized by binuclear zinc coordination with extensive outer-shell constraints. Besides a conserved Asp285 that bridges

two bound zinc ions 3.8 Å apart (Fig. 2d), each of the remaining coordinating residues (His232, His248, His283, and His261 from the neighboring subunit) is constrained through hydrogen bonds to neighboring residues, some of which can form bidentate hydrogen bonds with additional residues to establish an extensive network of outer-shell interactions at the CTD interface, thereby stabilizing the CTD-CTD association.

Electrostatic interactions at the dimer interface

One striking feature revealed at 2.9-Å resolution is a highly charged CTD interface stretching from the $(Lys77\text{-}Asp207)_2$ charge interlock on the cytoplasmic membrane surface to the tip of the CTD 30-Å into the cytoplasm (Fig. 3a). By contrast, the lipid-facing surface of YiiP is nearly devoid of charges (Fig. 3b). The clustered positive charges near the cytoplasmic membrane surface conform to the positive-inside-rule of membrane proteins31. The charge interlock and the TMD-TMD hydrophobic interactions in the inner leaflet of the membrane (Fig. 1a) hold the two positively-charged protein-surfaces together against their electrostatic repulsion. A transition from positive charges to clustering of negative charges surrounding site C provides a favorable electrostatic environment for binuclear zinc binding to the CTD interface (Fig. 3a). Upon zinc release from site C, we envision that the resulting electronegativity and side-chain rearrangements (e.g. H261 and H283) would cause two CTDs to swing apart due to charge repulsion and loss of inter-subunit contacts (Fig. 3c). As the CTD portion of the YiiP structure is essentially identical to the structure of a soluble fragment of a CDF homolog, CzrB, either in the presence or absence of zinc binding (Supplementary Fig. 6 online)32, the zinc-induced CTD conformational changes may be largely restricted to *en bloc* movements.

Zinc-induced conformational changes

Sited-directed FRET measurements were used to probe the putative inter-CTD movements in response to zinc binding. YiiP doubly-labeled with thiol-specific donor (Alexa-488) and acceptor (Alexa-647) fluorophores33 displayed pronounced FRET signals (see **Methods**). YiiP contains two indigenous cysteine residues: Cys127 and Cys287. Control experiments indicated that labeling $YiiP^{C287S}$ with the Alexa donor-acceptor pair did not produce detectable FRET signal. Furthermore, the FRET response from doubly labeled $YiiP^{C127V}$ was found nearly identical to that of YiiP. Thus the observed FRET change reflected the distance change between a pair of Cys287 residues located at the CTD interface (Fig. 4a). The inter-C287 distance is 24-Å in the crystal structure, well within the Förster radius (≈50-Å) for the Alexa-488 Alexa-647 pair. Zinc titrations of doubly-labeled YiiP showed a progressive increase of FRET (**Inset,** Fig. 4a), corresponding to a decrease of the inter-CTD distance. The observed distance change is specific to zinc binding because EDTA could fully reverse the FRET responses. Analytical sizing HPLC analysis of YiiP samples showed that proteins remained monodisperse before and after zinc titrations. However, a shift of peak retention time was detected, in agreement with a zinc-induced conformational change (data not shown). Moreover, a single H232A mutation in YiiP abolished the zinc-induced FRET responses (**Inset,** Fig. 4a). Since His232 is a conserved coordinating residue in site C (Fig. 2d), this result indicates that zinc binding to site C is required to bring together the Cys287 pair.

Allosteric regulation

To characterize the functional role of site C, we examined the effect of H232A mutation on zinc transport by stopped-flow fluorometry. As shown in Figure 4b, YiiP mediated a rapid Zn(II) influx into reconstituted proteoliposomes encapsulated with a Zn(II)-sensitive fluorescent indicator FluoZin-19. In comparison, YiiP^{H232A} showed reduced transport kinetics with approximately 2.2-fold increase of the Michaelis-Menten constant (K_M) and 2.0-fold decrease of the turnover rate (Supplementary Table 1 online). Thus, perturbation of site C could allosterically affect zinc transport via the active-site located 49-Å away from site C (Fig. 1a). It is worth noting that even a few fold changes in transport activity or protein expression can have significant pathological consequences34,35. Furthermore, a H232A mutation to site C was found causing approximately 5.7-fold decrease of thiol-reactivity of a reporter cysteine (D157C) in site A, in support of an allosteric connection between sites A and C (Supplementary Fig. 7 online).

A model for allosteric regulation

The YiiP structure provides a framework for understanding the allosteric mechanism. A flexible loop from residue Leu206 to Pro211 links CTD to TMD, reminiscent of a gating loop that connects ligand binding domain to the pore domain of ligand-gated channels36. This TMD-CTD connecting loop harbors the charge interlock that stabilizes dimer association regardless of zinc binding, because the zinc-free YiiP remains to be a homodimer28. Thus the charge interlock may serve as a pivotal point for a hinge-like motion between two CTDs in response to zinc binding to site C (Fig. 3c). As such, the charge interlock is well positioned to sense the inter-CTD movements and respond with alterations in TM3-TM6 orienting-constraints. As described above, the transmembrane sectors of TM3-TM6 are almost freely suspended in the lipid bilayer except for a packing contact with TM5 (Fig. 1c). Therefore, reorientations of the TM3-TM6 pairs can be directly coupled to reorientations of TM5. On the other hand, TM2 likely remains relatively static because its transmembrane sector hardly makes any inter-helical contact with the TM3-TM6 pair. A small shift of TM5 with respect to TM2, even in the order of an angstrom, would suffice to affect the coordination geometry of the active-site for zinc transport (Fig. 2b). This regulatory mechanism may be well conserved in the entire CDF family, as the TMD-CTD connecting loop and the four interlocking salt-bridges are among the most conserved structural components in YiiP (Supplementary Fig. 5 online).

The charge interlock is essential for zinc transport

A critical structural element in the putative allosteric pathway is the charge interlock. Mutation-activity analysis was performed to examine its functional role. A D207K mutation completely abolished YiiP expression, because introducing an extra positive-charge would destabilize dimer association between two positively-charged protein surfaces (Fig. 3a). In contrast, a K77D mutation only slightly reduced YiiP expression, attributing to the favorable electrostatic contribution of K77D to dimeric association. However, transport activity of the reconstituted YiiP^{K77D} was nearly reduced to a background level (Fig. 4b). Since the charge interlock plays a critical role in stabilizing the TM3-TM6 orientation (Fig. 1d), one possibility for the loss-of-function is the disorientation of the TM3-TM6 pair, which can be

transmitted to disrupting the tetrahedral coordination geometry of the active site. Indeed, a K77D/D207K double mutation restored transport activity (Fig. 4b).

DISCUSSION

Our findings suggest how metallochemistry may be tailored to achieve distinct functions in a metal transporter: a complete absence of outer-shell constraints gears up the active-site for rapid transport kinetics whereas the extensive outer-shell interactions surrounding the binuclear zinc binding-site allows effective zinc sensing via inter-CTD motions. These structural features support an auto-regulatory mechanism by which the *en bloc* movements of CTDs convert increasing cytoplasmic zinc concentrations to elevated efflux activities of YiiP, thereby removing excess zinc from the cytoplasm. Our study thus provides a first structural view into how a metallochaperone-like cytoplasmic domain regulates metal transport activity. The binding-sites involved in transport-regulation and in metal-trafficking18 are located on different faces of a metallochaperone-like protein, permitting a functional integration of transport regulation and metal trafficking in this structural module. Furthermore, evolution seems to select a common TMD-CTD modular architecture for the Ca^{2+}, Mg^{2+} and Zn^{2+} transporters37–41. The auto-regulatory mechanism proposed for YiiP may have broad implications for cation homeostatic controls at the membrane transporter level. Finally, homology modeling localized the most significant ZnT-8 genotype (R325W)23 to the CTD interface, highlighting the importance of the CTD interface as a drug action site.

METHODS

Crystallization

We carried out overexpression and purification of YiiP as described previously42. The purified sample was concentrated to 10∼15 mg ml^{-1}, and then dialyzed against a buffer containing 100 mM NaCl, 10 mM HEPES, 0.05% (w/v) n-undecyl-β-D-maltoside, 20% (w/v) Glycerol and 0.5 mM Tris(2-carboxyethyl) phosphine hydrochloride (TCEP), pH 7.0. After two weeks of dialysis at 4°C, the protein sample was mixed with an equal volume of a crystallization solution containing 100 mM Na-citrate (pH 6.0), 5 mM $ZnSO_4$, 3 mM Fos-Choline-12, 100 mM NaCl, 200 mM $(NH_4)_2SO_4$, 10% (v/v) PEG400, 15–20% (w/v) PEG2000, 4% (w/v) benzamidine, 10% (w/v) glycerol and 4% (v/v) 1,3-propanediol. YiiP crystals grew in hanging drops at 20°C, usually appeared after two weeks and continued to grow to full size in approximately one month.

Crystal derivatization and data collection

To derivatize crystals, we added ethyl mercury phosphate (0.5 mM), thiomerosal (0.5 mM) or $KAu(CN)_2$ (2 mM)+KI (300 mM) directly to the crystal drops. After incubating with heavy atoms for 2 to 24 hours at 20°C, crystals were harvested and flash-frozen in liquid nitrogen. More than 3, 000 crystals were pre-screened at beam-line X25 of the National Synchrotron Light Source. Only less than 1% of crystals showed good diffraction quality suitable for data collection. Diffraction data were processed using the program suite HKL200043. Data collected from 25 crystals were merged together to improve data quality.

Datasets collected from ethyl mercury phosphate, thiomerosal and $KAu(CN)_2$+KI derivatives are denoted as Hg1, Hg2 and "Au+I", respectively. Datasets Hg1 and Hg2 were further merged to form an "Hg1+Hg2" dataset. A previously collected dataset from native YiiP crystals13, designated as native in Table 1, was also used for structure determination.

Structure determination

We carried out molecular replacement to obtained initial phases using the program PHASER44 and a search model derived from the low resolution structure (PDB code 2QFI)13. The molecular replacement phases were used to locate mercury, gold and iodide positions. Model-derived phases were excluded thereafter from calculations of electron density maps. Rather, SIRAS phases were calculated using the program SHARP45. The SIRAS phases were then extended to 2.9-Å resolution by solvent flattering, temperature factor sharpening, non-crystallographic symmetry averaging and inter-crystal symmetry averaging with the *experimental* MIRAS-SAD phases derived for the native dataset13. The program suite CCP446 was employed for structural analysis unless stated otherwise. Density modification yielded an experimental electron density map of high quality (Supplementary Fig. 2 online). Subsequent manual rebuilding of the structural model was performed using the program O47, and structure refinement was accomplished using the program REFMAC48. All structure figures were prepared using the programs PyMol49 and RIBBONS50.

Site-directed FRET measurements

We incubated purified YiiP or $YiiP^{H232A}$ at a concentration of 40 μM in the dark for 60 min at 4 °C with 100 μM Alexa Fluor 488 C_5-maleimide and 100 μM Alexa Fluor 647 C_2-maleimide in a HPLC-buffer containing 100 mM NaCl, 10 mM HEPES, 0.05% (w/v) n-dodecyl-β-D-maltoside, 12% (w/v) Glycerol and 0.5 mM Tris(2-carboxyethyl) phosphine hydrochloride (TCEP), pH 7.0. The labeled proteins were then purified by sizing-exclusion HPLC to removed free Alexa dyes. The protein samples (0.5 μM) were excited at 490 nm and emission spectra from 500–700 nm were recorded on an ISS PC1 spectrofluorometer. Emission spectra showed two fluorescence maxima at 525 nm and 670 nm, corresponding to the Alexa-488 emission peak and the Alexa 488–647 FRET peak, respectively. In contrast, labeling YiiP with Alexa 488 or Alexa 647 alone showed no detectable FRET signal when excited at 490 nm. For zinc titration experiments, a Zn(II) stock solution was added sequentially to protein samples to a final concentration ranging from 0 to 3,200 μM. The emission spectrum recoded in the absence of Zn(II) was subtracted from the spectra recorded in the presence of Zn(II) to yield difference emission spectra (ΔF), which were then normalized to the Alex-488 emission peak intensity at 525 nm. The ratio of the normalized FRET intensity change $\Delta F/F$ at 670 nm to maximum $\Delta F/F$ at 3,200 μM Zn(II) yielded fractional $\Delta F/F$.

Stopped-flow transport assays

We performed stopped-flow transport experiments as described previously21. Briefly, YiiP and mutants were reconstituted into proteoliposomes, likely in mixed membrane orientations. Zinc uptake was elicited by an inwardly orientated zinc concentration gradient.

SDS-PAGE analysis of proteoliposome samples confirmed that approximately similar amounts of YiiP or mutants were reconstituted in each experiment. Empty-liposome traces were subtracted from the proteoliposome traces, and the resultant normalized kinetic traces were fitted to an exponential function using SigmaPlot 4.0 (SPSS Inc). The exponential responses of proteoliposomes, except the $YiiP^{k77D}$ proteoliposomes, were at least 5-fold above the background levels. The $YiiP^{k77D}$ signals were only slightly above the background levels, precluding further analysis because parameter-fitting was not reliable. The transport turnover rate k and Michaelis-Menten constant K_M values were obtained by fitting the exponential rate constant (k_i) to the Zn(II) concentration according to the equation: $k_i = k[\text{Zn(II)}]/(K_M + [\text{Zn(II)}])$.

Supplementary Material

Refer to Web version on PubMed Central for supplementary material.

Acknowledgements

We thank the staff at beamline X25 of National Synchrotron Light Source of Brookhaven Nation Laboratory for technical assistance during data collection. We also thank J. Shanklin, P. Freimuth, B.P. Rosen, C. Anderson, C. Correll, R. Kaplan and D. Mueller for critically reading the manuscript. This work was supported by the National Institute of Health (to D.F.), Office of Basic Energy Sciences, Department of Energy (to D.F.) and the Biology Department of Brookhaven National Laboratory.

References

1. Vallee BL, Falchuk KH. The biochemical basis of zinc physiology. Physiol Rev. 1993; 73:79–118. [PubMed: 8419966]
2. Berg J, Shi Y. The galvanization of biology: a growing appreciation for the roles of zinc. Science. 1996; 271:1081–1085. [PubMed: 8599083]
3. Koh JY, et al. The role of zinc in selective neuronal death after transient global cerebral ischemia. Science. 1996; 272:1013–1016. [PubMed: 8638123]
4. Outten C, O'Halloran T. Femtomolar sensitivity of metalloregulatory proteins controlling zinc homeostasis. Science. 2001; 292:2488–2492. [PubMed: 11397910]
5. Zhao H, Eide D. The yeast ZRT1 gene encodes the zinc transporter protein of a high-affinity uptake system induced by zinc limitation. Proc Natl Acad Sci U S A. 1996; 93:2454–2458. [PubMed: 8637895]
6. Grotz N, et al. Identification of a family of zinc transporter genes from *Arabidopsis* that respond to zinc deficiency. Proc Natl Acad Sci U S A. 1998; 95:7220–7224. [PubMed: 9618566]
7. Palmiter R, Findley S. Cloning and functional characterization of a mammalian zinc transporter that confers resistance to zinc. EMBO Journal. 1995; 14(4):639–649. [PubMed: 7882967]
8. Nies DH, Silver S. Ion efflux systems involved in bacterial metal resistances. J Ind Microbiol. 1995; 14:186–199. [PubMed: 7766211]
9. Chao Y, Fu D. Kinetic Study of the Antiport Mechanism of an *Escherichia coli* Zinc Transporter, ZitB. J Biol Chem. 2004; 279:12043–12050. [PubMed: 14715669]
10. Ohana E, et al. Identification of the Zn^{2+} binding site and mode of operation of a mammalian Zn^{2+} transporter. J Biol Chem. 2009; 284:17677–17686. [PubMed: 19366695]
11. Cousins RJ, Liuzzi JP, Lichten LA. Mammalian zinc transport, trafficking, and signals. J Biol Chem. 2006; 281:24085–24089. [PubMed: 16793761]
12. Nies DH. How cells control zinc homeostasis. Science. 2007; 317:1695–1696. [PubMed: 17885121]
13. Lu M, Fu D. Structure of the zinc transporter YiiP. Science. 2007; 317:1746–1748. [PubMed: 17717154]

14. Wei Y, Fu D. Selective metal binding to a membrane-embedded aspartate in the *Escherichia coli* metal transporter YiiP (FieF). J Biol Chem. 2005; 280:33716–33724. [PubMed: 16049012]
15. Paulsen I, Saier MJ. A novel family of ubiquitous heavy metal ion transport proteins. Journal of Membrane Biology. 1997; 156(2):99–103. [PubMed: 9075641]
16. O'Halloran TV, Culotta VC. Metallochaperones, an intracellular shuttle service for metal ions. J Biol Chem. 2000; 275:25057–25060. [PubMed: 10816601]
17. Arnesano F, et al. Metallochaperones and metal-transporting ATPases: a comparative analysis of sequences and structures. Genome Res. 2002; 12:255–271. [PubMed: 11827945]
18. Rosenzweig AC, O'Halloran TV. Structure and chemistry of the copper chaperone proteins. Curr Opin Chem Biol. 2000; 4:140–147. [PubMed: 10742187]
19. Gonzalez-Guerrero M, Arguello JM. Mechanism of Cu^+-transporting ATPases: soluble Cu^+ chaperones directly transfer Cu^+ to transmembrane transport sites. Proc Natl Acad Sci U S A. 2008; 105:5992–5997. [PubMed: 18417453]
20. Hsi G, Cox DW. A comparison of the mutation spectra of Menkes disease and Wilson disease. Hum Genet. 2004; 114:165–172. [PubMed: 14579150]
21. Chimienti F, et al. *In vivo* expression and functional characterization of the zinc transporter ZnT8 in glucose-induced insulin secretion. J Cell Sci. 2006; 119:4199–4206. [PubMed: 16984975]
22. Scott LJ, et al. A genome-wide association study of type 2 diabetes in Finns detects multiple susceptibility variants. Science. 2007; 316:1341–1345. [PubMed: 17463248]
23. Sladek R, et al. A genome-wide association study identifies novel risk loci for type 2 diabetes. Nature. 2007; 445:881–885. [PubMed: 17293876]
24. Wenzlau JM, et al. The cation efflux transporter ZnT8 (Slc30A8) is a major autoantigen in human type 1 diabetes. Proc Natl Acad Sci U S A. 2007; 104:17040–17045. [PubMed: 17942684]
25. Zeggini E, et al. Replication of genome-wide association signals in UK samples reveals risk loci for type 2 diabetes. Science. 2007; 316:1336–13341. [PubMed: 17463249]
26. Finney LA, O'Halloran TV. Transition metal speciation in the cell: insights from the chemistry of metal ion receptors. Science. 2003; 300:931–936. [PubMed: 12738850]
27. Laskowski R, MacArthur M, Moss D, Thornton J. PROCHECK: A program to check the stereochemical quality of protein structures. J. Appl. Cryst. 1993; 26:283–291.
28. Wei Y, Li H, Fu D. Oligomeric state of the *Escherichia coli* metal transporter YiiP. J. Biol. Chem. 2004; 279:39251–39259. [PubMed: 15258151]
29. Grass G, et al. FieF (YiiP) from *Escherichia coli* mediates decreased cellular accumulation of iron and relieves iron stress. Arch Microbiol. 2005; 183:9–18. [PubMed: 15549269]
30. Frausto da Silva, J.; Williams, R. The biological chemistry of the elements-The inorganic chemistry of life. Oxford University Press; 2001. p. 315-333.
31. von Heijne G. Membrane-protein topology. Nat Rev Mol Cell Biol. 2006; 7:909–918. [PubMed: 17139331]
32. Cherezov V, et al. Insights into the mode of action of a putative zinc transporter CzrB in *Thermus thermophilus*. Structure. 2008; 16:1378–1388. [PubMed: 18786400]
33. Majumdar DS, et al. Single-molecule FRET reveals sugar-induced conformational dynamics in LacY. Proc Natl Acad Sci U S A. 2007; 104:12640–12645. [PubMed: 17502603]
34. de Bie P, Muller P, Wijmenga C, Klomp LW. Molecular pathogenesis of Wilson and Menkes disease: correlation of mutations with molecular defects and disease phenotypes. J Med Genet. 2007; 44:673–688. [PubMed: 17717039]
35. Murphy DL, Lesch KP. Targeting the murine serotonin transporter: insights into human neurobiology. Nat Rev Neurosci. 2008; 9:85–96. [PubMed: 18209729]
36. Sine SM, Engel AG. Recent advances in Cys-loop receptor structure and function. Nature. 2006; 440:448–455. [PubMed: 16554804]
37. Besserer GM, et al. The second Ca^{2+}-binding domain of the Na^+ Ca^{2+} exchanger is essential for regulation: crystal structures and mutational analysis. Proc Natl Acad Sci U S A. 2007; 104:18467–18472. [PubMed: 17962412]
38. Eshaghi S, et al. Crystal structure of a divalent metal ion transporter CorA at 2.9 angstrom resolution. Science. 2006; 313:354–257. [PubMed: 16857941]

39. Hattori M, Tanaka Y, Fukai S, Ishitani R, Nureki O. Crystal structure of the MgtE Mg^{2+} transporter. Nature. 2007; 448:1072–1075. [PubMed: 17700703]
40. Lunin VV, et al. Crystal structure of the CorA Mg^{2+} transporter. Nature. 2006; 440:833–937. [PubMed: 16598263]
41. Payandeh J, Pai EF. A structural basis for Mg^{2+} homeostasis and the CorA translocation cycle. EMBO J. 2006; 25:3762–3773. [PubMed: 16902408]
42. Chao Y, Fu D. Thermodynamic studies of the mechanism of metal binding to the *Escherichia coli* zinc transporter YiiP. J Biol Chem. 2004; 279:17173–17180. [PubMed: 14960568]
43. Otwinowski Z, Minor W. Processing of X-ray Diffraction Data Collected in Oscillation Mode. Methods Enzymol. 1997; 276:307–326.
44. Read RJ. Pushing the boundaries of molecular replacement with maximum likelihood. Acta Crystallogr D Biol Crystallogr. 2001; 57:1373–1382. [PubMed: 11567148]
45. De La Fortelle E, Bricogne G. Maximum-likelihood heavy-atom parameter refinement for multiple isomorphous replacement and multiwavelength anomalous diffraction methods. Methods Enzymol. 1997; 276:472–494.
46. The CCP4 suite: programs for protein crystallography. Acta Crystallogr D Biol Crystallogr. 1994; 50:760–763. [PubMed: 15299374]
47. Jones TA, Zou JY, Cowan SW, Kjeldgaard M. Improved methods for building protein models in electron density maps and the location of errors in these models. Acta Crystallogr A. 1991; 47:110–119. [PubMed: 2025413]
48. Murshudov GN, Vagin AA, Dodson EJ. Refinement of macromolecular structures by the maximum-likelihood method. Acta Crystallogr D Biol Crystallogr. 1997; 53:240–255. [PubMed: 15299926]
49. Delano WL. The PyMol molecular graphics system on the world wide web. 2002(htttp://www.pymol.org)
50. Carson M. Ribbsons. Methods Enzymol. 1987; 277:493–505. [PubMed: 18488321]

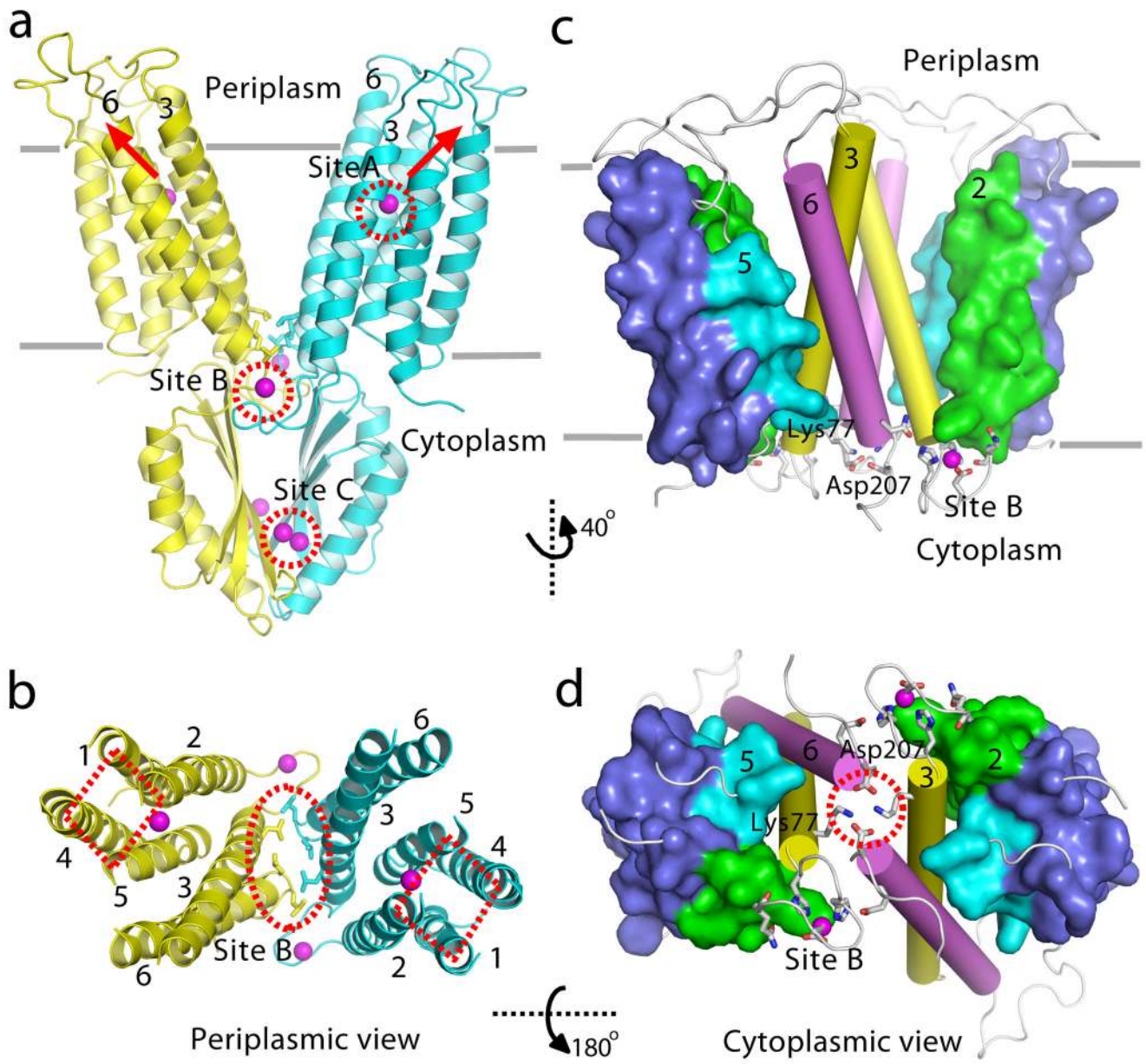

Figure 1.

YiiP structure and helix-packing in the transmembrane domain (TMD). (a) Ribbon representation of YiiP homodimer (yellow and cyan for each protomer) viewed from the membrane plane. Magenta spheres represent bound zinc ions in zinc binding-sites marked by red circles. Grey lines indicate the possible membrane boundaries. Red arrows indicate the directions of Zn(II) exit from the two active-sites. Conserved hydrophobic residues involved in the TMD-TMD contacts are shown as sticks. (b) YiiP homodimer viewed from the periplasm with extracellular loops and the cytoplasmic domain (CTD) removed for clarity. Red oval marks hydrophobic interactions at the TMD-TMD interface and red diamonds highlight four-helix bundles. (c) Packing of the TM3-TM6 pairs in the membrane.

TMDs are viewed from the membrane plane and related to (a) with a 40°-rotation about the dimer two-fold axis. TM3-TM6 pairs are shown in cylinder representation while the four-helix-bundle in solvent-accessible surface. (d) The charge interlock at the dimer interface is highlighted with a red circle and viewed from the cytoplasm with CTD removed for clarity.

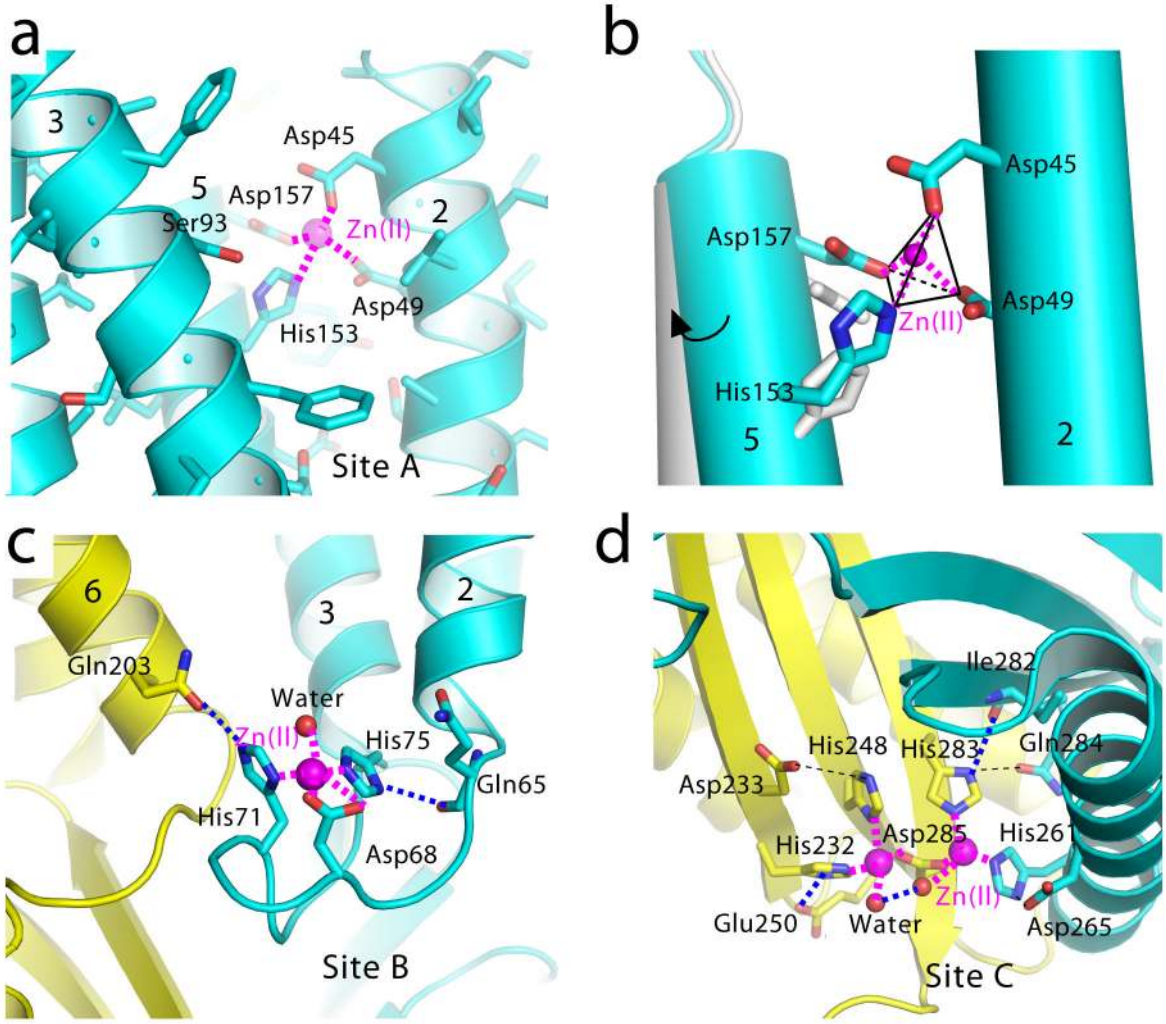

Figure 2.

Zinc binding sites. (a) Site A and its coordination environment shown in a 20-Å cross-section centered at a coordinated Zn(II) (magenta sphere). Magenta dashed-lines represent zinc-ligand coordination. (b) Regulation of coordination geometry. A close-up view of site A situated between TM2 and TM5 (cyan cylinders) with four coordinating residues (cyan sticks) in a tetrahedral arrangement (shown as a tetrahedron). A black arrow indicates a hypothesized TM5 movement (shown as a grey cylinder) with respect to TM2. (c) Site B. The red sphere represents a coordinated water molecule and blue dashed-lines indicate hydrogen bonds. (d) Site C and its outer-shell interactions. Grey dashed-lines indicate potential hydrogen bonds.

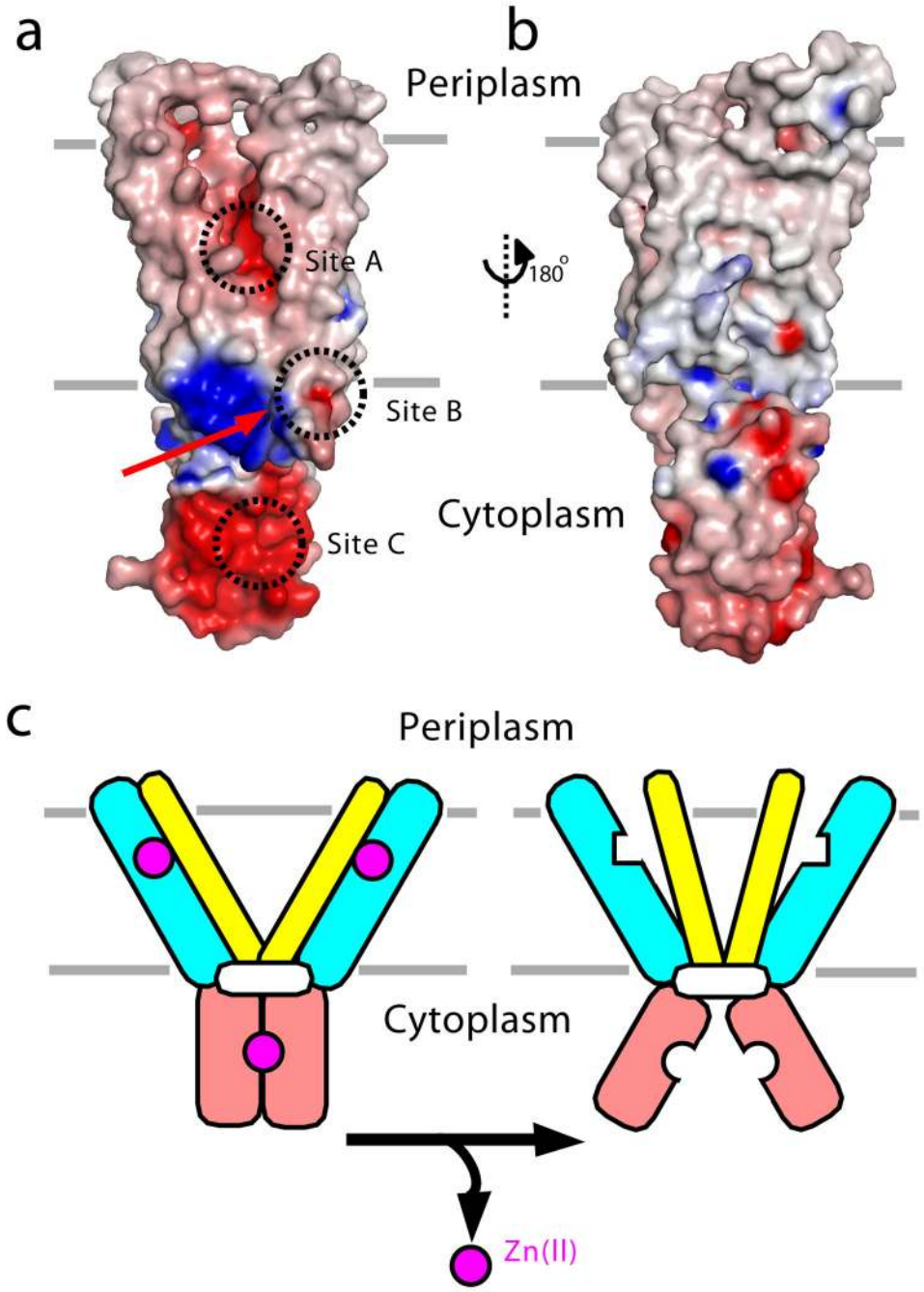

Figure 3.

Electrostatic surface potentials and a model for autoregulation. (a) Dimer interface viewed from the membrane plane. Protein surfaces are colored according to electrostatic potentials from −20 kTe^{-1} (red) to +20 kTe^{-1} (blue). Red arrow indicates the location of the charge interlock. (b) Lipid-facing surface viewed with an 180°-rotation of the YiiP protomer as indicated. (c) Schematic model for auto-regulation. TM3-TM6 pairs and four-helix bundles are colored in yellow and cyan, respectively. Open box represents the charge interlock located at the pivotal point of hinge-like motions.

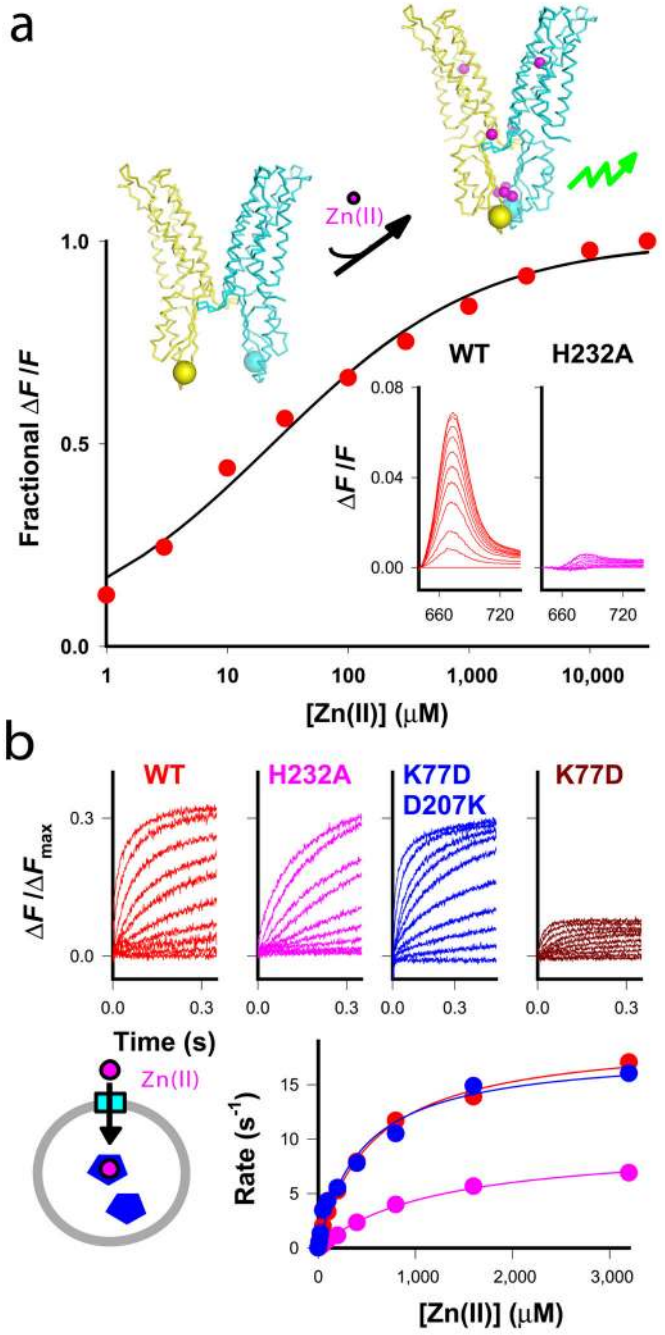

Figure 4.

Functional characterization (a) Zinc-induced inter-Cys287 distance changes. The ribbon drawing shows that a hypothetical inter-subunit motion alters the distance between a pair of donor and acceptor fluorophores labeled to two Cys287 residues (yellow and cyan spheres, respectively). The fractional FRET change obtained from YiiP was plotted as a function of the zinc concentration. The solid line represents a least-squares fit to the Hill-equation, yielding an apparent binding affinity of 24±3 μM with negative cooperativity (n=0.5±0.1). Insets, FRET spectra in response to zinc titrations obtained from doubly-labeled YiiP and

YiiP^{H232A} as indicated. (b) Zinc influxes into proteoliposomes in response to rapid additions of extravesicular Zn(II). Purified proteins as indicated were reconstituted and a zinc-sensitive fluorescent dye was encapsulated to monitor zinc influxes. The rate of zinc influx is plotted as a function of the zinc concentration. Solid lines represent least-squares fits to a hyperbolic equation with fitting parameters (K_M and k) given in Supplementary Table 1 online.

Table 1

Data collection, phasing and refinement statistics

	Hg1+Hg2[a]	Au+I	Native[8]
Data collection			
Space group	$P2_1$	$P2_1$	$P222_1$
Cell dimensions			
a, *b*, *c* (Å)	105.7, 130.7, 115.8	107.3, 131.3, 114.4	106.7, 110.8, 130.7
α, β, γ (°)	90, 93.3, 90	90, 92.0, 90	90, 90, 90
Resolution (Å)	50–2.9 (3.0–2.9)[b]	30–4.2 (4.4–4.2)	30–3.8 (3.9–3.8)
R_{sym} or R_{merge} (%)	5.9 (42.4)	10.8 (43.3)	12.9 (42.9)
$I / \sigma I$	18.6 (1.4)	9.3 (1.8)	13.3 (1.9)
Completeness (%)	92.7 (54.3)	69.7 (34.5)	97.3 (91.9)
Redundancy	3.6 (1.7)	2.6 (1.3)	6.8 (2.3)
Refinement			
Resolution (Å)	20–2.9		15–3.8
No. reflections	61,831		14,730
R_{work} / R_{free} (%)	26.1/27.7		30.2/30.3
No. atoms			
Protein	8,712		4,356
Ligand/ion	24		7
Water	265		
B-factors			
Protein	70.5		269.4
Ligand/ion	24.8		91.7
Water	30.1		
R.m.s deviations			
Bond lengths (Å)	0.009		0.013
Bond angles (°)	1.45		1.54

[a] Twenty five crystals were used.

[b] Values in parentheses are for highest-resolution shell.